

1 **Tropopause Evolution in a Rapidly Intensifying Tropical Cyclone: A Static**  
2 **Stability Budget Analysis in an Idealized, Axisymmetric Framework**

3 Patrick Duran\* and John Molinari

4 *University at Albany, State University of New York, Albany, NY*

5 \**Corresponding author address:* Department of Atmospheric and Environmental Sciences, Univer-  
6 sity at Albany, State University of New York, 1400 Washington Avenue, Albany, NY.

7 E-mail: pduran2008@gmail.com

## ABSTRACT

8 Large changes in tropopause-layer static stability are observed during the  
9 rapid intensification (RI) of an idealized, axisymmetric tropical cyclone (TC).  
10 Over the eye, static stability near the tropopause decreases and the cold-point  
11 tropopause height rises by up to 4 km at the storm center. Outside of the eye,  
12 static stability immediately above the cold-point tropopause increases consid-  
13 erably, and the tropopause remains near its initial level. A budget analysis  
14 reveals that advection contributes to the static stability tendencies at all times  
15 throughout the upper troposphere and lower stratosphere. Advection is partic-  
16 ularly important within the eye, where it acts to destabilize the layer near and  
17 above the cold-point tropopause. Outside of the eye, a radial-vertical circula-  
18 tion develops during RI, with strong outflow below the tropopause and weak  
19 inflow above. Vertical wind shear above and below the upper-tropospheric  
20 outflow maximum induces turbulence, which provides forcing for both desta-  
21 bilization and stabilization in the tropopause layer. Meanwhile, as organized  
22 convection reaches the tropopause, radiative heating tendencies at the top of  
23 the cirrus canopy generally act to destabilize the upper troposphere and stabi-  
24 lize the lower stratosphere. Turbulent mixing and radiative heating combine  
25 to play an important role in the development of the strong stable layer im-  
26 mediately above the cold-point tropopause during RI. The results suggest that  
27 turbulence and radiation, alongside advection, play fundamental roles in the  
28 upper-level static stability evolution of TCs.

## 29 **1. Introduction**

30 After undergoing a remarkably rapid intensification (RI), Hurricane Patricia (2015) set a new  
31 record as the strongest tropical cyclone (TC) ever observed in the Western Hemisphere (Kim-  
32 berlain et al. 2016; Rogers et al. 2017). High-altitude dropsonde observations taken during the  
33 Tropical Cyclone Intensity (TCI) experiment captured this RI in unprecedented detail (Doyle et al.  
34 2017). These observations revealed dramatic changes in the structure of the cold-point tropopause  
35 and upper-level static stability as the storm intensified (Duran and Molinari 2018).

36 At tropical storm intensity, shortly before RI commenced, a strong inversion layer existed just  
37 above Patricia’s cold-point tropopause, which was located near 17.2 km. During the first half of  
38 the RI period, this inversion layer weakened throughout Patricia’s inner core, with the weakening  
39 most pronounced over the developing eye. By the time the storm reached its maximum intensity,  
40 the inversion layer over the eye had disappeared almost completely, which was accompanied by an  
41 increase in the tropopause height to a level at or above the highest-available dropsonde data point  
42 (18.3 km) at two locations. Meanwhile over the eyewall region, the static stability re-strengthened  
43 and the tropopause was limited to a level at or below 17.5 km. The mechanisms that led to these  
44 changes in upper-level static stability and tropopause height are the subject of the current paper.

45 Despite the importance of tropopause-layer thermodynamics in theoretical models of hurricanes  
46 (Emanuel and Rotunno 2011; Emanuel 2012), few papers have examined the upper-tropospheric  
47 evolution of TCs. Komaromi and Doyle (2017) found that stronger TCs tended to have a higher  
48 and warmer tropopause over their inner core than weaker TCs. Their results are consistent with  
49 the evolution observed over the inner core of Hurricane Patricia, in which the tropopause height  
50 increased and the tropopause temperature warmed throughout RI (Duran and Molinari 2018).

51 Idealized simulations of a TC analyzed by Ohno and Satoh (2015) suggested that the develop-  
52 ment of an upper-level warm core near the TC storm center acted to decrease the static stability  
53 near the tropopause (see their Fig. ). Although the mechanisms that drive this static stability  
54 evolution have not been examined explicitly, Stern and Zhang (2013) described the development  
55 of the TC warm core using a potential temperature ( $\theta$ ) budget analysis. They found that radial  
56 and vertical advection both played important roles in warm core development throughout RI, and  
57 subgrid-scale diffusion became particularly important during the later stage of RI. To our knowl-  
58 edge, the only paper that has examined explicitly the static stability evolution in a modeled TC is  
59 Kepert et al. (2016), but their analysis was limited to the boundary layer. The analysis herein is  
60 based upon that of Stern and Zhang (2013), except using a static stability budget similar to that of  
61 Kepert et al. (2016), with a focus on the upper troposphere and lower stratosphere.

## 62 **2. Model Setup**

63 The numerical simulations were performed using version 19.4 of Cloud Model 1 (CM1) de-  
64 scribed in Bryan and Rotunno (2009). The equations of motion were integrated on a 3000-km-  
65 wide, 30-km-deep axisymmetric grid with 1-km horizontal and 250-m vertical grid spacing. The  
66 computations were performed on an  $f$ -plane at 15°N latitude, over a sea surface with constant  
67 temperature of 30.5°C, which matches that observed near Hurricane Patricia (2015; Kimberlain  
68 et al. 2016). Horizontal turbulence was parameterized using the Smagorinsky scheme described in  
69 Bryan and Rotunno (2009, pg. 1773), with a prescribed mixing length that varied linearly from 100  
70 m at a surface pressure of 1015 hPa to 1000 m at a surface pressure of 900 hPa. This formulation  
71 allows for realistically-large horizontal mixing lengths near the hurricane’s inner core, consistent  
72 with the results of Bryan (2012), while not over-representing horizontal turbulence in convection  
73 at outer radii. Vertical turbulence was parameterized using the formulation of Markowski and

74 Bryan (2016, their Eq. 6), using an asymptotic vertical mixing length of 100 m. A Rayleigh  
75 damping layer was applied outside of the 2900-km radius and above the 25-km level to prevent  
76 spurious gravity wave reflection at the model boundaries. Microphysical processes were param-  
77 eterized using the Thompson et al. (2004) microphysics scheme and radiative heating tendencies  
78 were computed every two minutes using the Rapid Radiative Transfer Model for GCMs (RRTMG)  
79 longwave and shortwave schemes (Iacono et al. 2008). The initial temperature and humidity field  
80 was horizontally homogeneous and determined by averaging all Climate Forecast System Reanal-  
81 ysis (CFSR) grid points within 100 km of Patricia's center of circulation at 18 UTC 21 October  
82 2015. The vortex described in Rotunno and Emanuel (1987, their Eq. 37) was used to initialize  
83 the wind field, setting all parameters equal to the values used therein.

84 Although hurricanes simulated in an axisymmetric framework tend to be more intense than  
85 those observed in nature, the intensity evolution of this simulation matches reasonably well with  
86 that observed in Hurricane Patricia. After an initial spin-up period of about 20 hours, the modeled  
87 storm (Fig.1, blue lines) began an RI period that lasted approximately 30 hours. After this RI, the  
88 storm continued to intensify more slowly until the maximum 10-m wind speed reached  $89 \text{ m s}^{-1}$   
89 and the minimum sea-level pressure reached its minimum of 846 mb, 81 hours into the simulation.  
90 Hurricane Patricia (red stars) exhibited a similar intensity evolution, with an RI period leading to a  
91 maximum 10-m wind speed of  $95 \text{ m s}^{-1}$  and a minimum sea-level pressure of 872 hPa. Despite the  
92 limitations of the axisymmetric framework, the extraordinary intensity of Hurricane Patricia and  
93 the rapidity of its intensification makes Patricia a particularly good candidate for axisymmetric  
94 analysis.

### 95 3. Budget Computation

96 The static stability can be expressed as the squared Brunt Väisälä frequency:

$$N_m^2 = \frac{g}{T} \left( \frac{\partial T}{\partial z} + \Gamma_m \right) \left( 1 + \frac{T}{R_d/R_v + q_s} \frac{\partial q_s}{\partial T} \right) - \frac{g}{1 + q_t} \frac{\partial q_t}{\partial z}, \quad (1)$$

97 where  $g$  is gravitational acceleration,  $T$  is temperature,  $R_d$  and  $R_v$  are the gas constants of dry air  
 98 and water vapor, respectively,  $q_s$  is the saturation mixing ratio,  $q_t$  is the total condensate mixing  
 99 ratio, and  $\Gamma_m$  is the moist-adiabatic lapse rate:

$$\Gamma_m = g(1 + q_t) \left( \frac{1 + L_v q_s / R_d T}{c_{pm} + L_v \partial q_s / \partial T} \right), \quad (2)$$

100 where  $L_v$  is the latent heat of vaporization and  $c_{pm}$  is the specific heat of moist air at constant  
 101 pressure. In the tropopause layer,  $q_s$ ,  $\partial q_s / \partial T$ , and  $\partial q_t / \partial z$  approach zero. In this limiting case,  
 102 Eq. 1 reduces to:

$$N^2 = \frac{g}{\theta} \frac{\partial \theta}{\partial z}, \quad (3)$$

103 where  $\theta$  is the potential temperature.

104 To compute  $N^2$ , CM1 uses Eq.1 in saturated environments and Eq. 3 in sub-saturated environ-  
 105 ments. For simplicity, however, only Eq. 3 will be employed for the budget computations herein<sup>1</sup>.

106 Taking the time derivative of Eq. 3 yields the static stability tendency:

$$\frac{\partial N^2}{\partial t} = \frac{g}{\theta} \frac{\partial}{\partial z} \frac{\partial \theta}{\partial t} - \frac{g}{\theta^2} \frac{\partial \theta}{\partial z} \frac{\partial \theta}{\partial t}, \quad (4)$$

107 where the potential temperature tendency,  $\partial \theta / \partial t$ , can be written:

$$\frac{\partial \theta}{\partial t} = HADV + VADV + HTURB + VTURB + MP + RAD + DISS \quad (5)$$

108 Each term on the right-hand side of Eq. 5 represents a  $\theta$  budget variable, each of which is out-  
 109 put directly by the model every minute. HADV and VADV are the radial and vertical advective

---

<sup>1</sup>The validity of this approximation will be substantiated later in this section.

tendencies<sup>2</sup>, HTURB and VTURB are the radial and vertical tendencies from the turbulence parameterization, MP is the tendency from the microphysics scheme, RAD is the tendency from the radiation scheme, and DISS is the tendency due to turbulent dissipation. This equation neglects Rayleigh damping, since this term is zero everywhere below 25 km, and the analysis domain does not extend to that level. Each term in Eq. 5 is substituted for  $\partial\theta/\partial t$  in Eq. 4, yielding the contribution of each budget term to the static stability tendency. These terms are summed, yielding an instantaneous "budget change" in  $N^2$  every minute. The budget changes are then averaged over 24-hour periods and compared to the total model change in  $N^2$  over that same time period, i.e.:

$$\Delta N_{budget}^2 = \frac{1}{\delta t} \sum_{t=t_0}^{t_0+\delta t} \left. \frac{\partial N^2}{\partial t} \right|_t \quad (6)$$

$$\Delta N_{model}^2 = N_{t_0+\delta t}^2 - N_{t_0}^2 \quad (7)$$

$$Residual = \Delta N_{model}^2 - \Delta N_{budget}^2 \quad (8)$$

where  $t_0$  is an initial time and  $\delta t$  is 24 hours.

Eqs. 6-8 are plotted for four consecutive 24-hour periods in Fig. 2. For this and all subsequent radial-vertical cross sections, a 1-2-1 smoother is applied once in the radial direction to eliminate  $2\Delta r$  noise that appears in some of the raw model output and calculated fields. The left column of Fig. 2 depicts the model changes (Eq. 7), the center column depicts the budget changes (Eq. 6), and the right column depicts the residuals (Eq. 8). In every 24-hour period, the budget changes are nearly identical to the model changes, which is reflected in the near-zero residuals in the right column. This indicates that the budget accurately represents the model variability, which implies that the neglect of moisture in the budget computation introduces negligible error within the analysis domain<sup>3</sup>.

---

<sup>2</sup>These terms include the tendencies due to the diffusion that is implicit in the fifth-order advection scheme.

<sup>3</sup>This is not the case in the lower- and mid-troposphere, where the residual actually exceeds the budget variability in many places, likely due to the neglect of moisture; thus we limit this analysis to the upper troposphere and lower stratosphere.

130 In the tropopause layer, some of the budget terms are small enough to be ignored. To determine  
131 which of the budget terms are most important, a time series of the contribution of each of the  
132 budget terms in Eq. 5 to the tropopause-layer static stability tendency is plotted in Fig. 4. For this  
133 figure, each of the budget terms is computed using the method described in Section 3, except with  
134 1-hour averaging intervals instead of 24-hour intervals. The absolute values of these tendencies  
135 are then averaged over a radius-height domain surrounding the tropopause and plotted as a time  
136 series<sup>4</sup>. Advection (Fig. 4, red line) plays an important role in the mean tropopause-layer static  
137 stability tendency at all times, and vertical turbulence (Fig. 4, blue line) and radiation (Fig. 4, dark  
138 green line) also contribute significantly. Although the contribution from horizontal turbulence  
139 (Fig. 4, purple line) becomes more important after 48 hours, it is confined to a very small region  
140 immediately surrounding the eyewall tangential velocity maximum (not shown), and is negligible  
141 throughout the rest of the tropopause layer. The remaining two processes - microphysics and  
142 dissipative heating (Fig. 4, orange and light green lines, respectively) - lie atop one another near  
143 zero. These time series indicate that, at all times, three budget terms dominate the tropopause-layer  
144 static stability tendency: advection, vertical turbulence, and radiation. Variations in the magnitude  
145 and spatial structure of these terms drive the static stability changes depicted in Fig. 2; subsequent  
146 sections will focus on these variations and what causes them.

---

<sup>4</sup>It will be seen in subsequent figures that each of the terms contributes both positively and negatively to the  $N^2$  tendency within the analysis domain. Thus, taking an average over the domain tends to wash out the positive and negative contributions. To circumvent this problem, the absolute value of each of the terms is averaged.



## 4. Results

### *a. Static stability evolution*

The average  $N^2$  over the first day of the simulation (Fig. 3a) indicates the presence of a weak static stability maximum just above the cold-point tropopause. Over the subsequent 24 hours, during the RI period, the static stability within and above this layer decreased near the storm center (Fig. 3b). This decreasing  $N^2$  corresponded to an increase in the tropopause height within the developing eye, maximized at the storm center. Outside of the eye, meanwhile, the tropopause height decreased over the eyewall region (25-60-km radius) and increased only slightly outside of the 60-km radius. In this outer region, the  $N^2$  maximum just above the tropopause strengthened during RI. These trends continued as the storm's intensity leveled off in the 48-72-hour period (Fig. 3c). The tropopause height increased to nearly 21 km at the storm center and sloped sharply downward to 16.3 km on the inner edge of the eyewall, near the 30 km radius. Static stability outside of the eye, meanwhile, continued to increase just above the cold-point tropopause. This  $N^2$  evolution closely follows that observed in Hurricane Patricia (2015; Duran and Molinari 2018). The mechanisms that led to these static stability changes will be investigated in the subsequent sections.

### *b. Static stability budget analysis*

*(i) 0-24 hours* The weakening of the lower-stratospheric static stability maximum during the initial spin-up period is reflected in the total  $N^2$  budget change over this time (Fig. 5a). The 17-18-km layer was characterized by decreasing  $N^2$  (purple shading), maximizing at the storm center. The layer immediately below the tropopause, meanwhile, saw strengthening  $N^2$  during this time period. Although these tendencies extended out to the 200-km radius, they were particularly

pronounced at innermost radii. A comparison of the contributions of advection (Fig. 5b), vertical turbulence (Fig. 5c), and radiation (Fig. 5d) reveals that advection is primarily responsible for the change in static stability during this period. Although vertical turbulence acts in opposition to advection (i.e. it acts to stabilize regions that advection acts to destabilize), the magnitude of the advective tendencies is larger, particularly at the innermost radii. The sum of advection and vertical turbulence (Fig. 5e) almost exactly replicates the static stability tendencies above 17 km. Radiative tendencies (Fig. 5d) act to destabilize the layer below about 16 km and stabilize the layer between 16 and 17 km. The sum of advection, vertical turbulence, and radiation (Fig. 5f) reproduces the total change in  $N^2$  almost exactly.

...Explain this in the context of radial and vertical velocities... ...See Stern and Zhang, Page 84, Section 3d... ...Add mention of total condensate and radiative heating tendencies as it relates to stability tendency due to rad...

(ii) *24-48 hours* During the RI period,  $N^2$  within the eye generally decreased above 16 km and increased below (Fig. 6a). These tendencies at the innermost radii were driven almost entirely by advection (Fig. 6b); vertical turbulence (Fig. 6c) and radiation (Fig. 6d) contributed negligibly to the static stability tendencies in this region.

Outside of the eye, the  $N^2$  evolution exhibited alternating layers of positive and negative tendencies. Near and above 18 km existed an upward-sloping region of decreasing  $N^2$  that extended out to the 180-km radius. In this region, neither vertical turbulence nor radiation exhibited negative  $N^2$  tendencies; advection was the only forcing for destabilization. Immediately below this layer was a region of increasing  $N^2$ , which sloped upward from 17 km near the 30-km radius to just below 18 km outside of the 100-km radius. Advection and vertical turbulence both contributed to this positive  $N^2$  tendency, with advection playing an important role below about 17.5 km and and

192 turbulence playing an important role above. The sum of advection and turbulence (Fig. 6e) reveals  
 193 two discontinuous regions of increasing  $N^2$  in the 17-18-km layer rather than one contiguous re-  
 194 gion. The addition of radiation to these two terms, however, (Fig. 6f) provides the link between  
 195 these two regions, indicating that radiation also plays a role in strengthening the stable layer just  
 196 above the tropopause. In the 16-17-km layer, a horizontally-extensive layer of decreasing  $N^2$  also  
 197 was forced by a combination of advection, vertical turbulence, and radiation. The sum of advec-  
 198 tion and vertical turbulence accounts for only a portion of the decreasing  $N^2$  in this layer, and  
 199 actually indicates forcing for stabilization near the 50-km radius and outside of the 130-km radius.  
 200 Radiative tendencies overcome this forcing for stabilization in both of these regions to produce the  
 201 radially-extensive region of destabilization observed just below the tropopause.

202 TWO REGIONS WHERE Panel (f) differs from panel (a): 30-60 km radial band below 16 km,  
 203 which is actually canceled out by a vertical gradient of latent heating, and the thin region of strong  
 204 stabilization between 15-17.5 km near  $r=30$  km, which is canceled out by horizontal turbulence.

205 (iii) 48-72 hours After the storm's maximum wind speed leveled off near  $80 \text{ m s}^{-1}$ , the magnitude  
 206 of the static stability tendencies within the eye decreased to near zero (Fig. 7a).

207 Outside of the eye, however,  $N^2$  continued to increase just above the tropopause and decrease  
 208 just below. The sum of advection and vertical turbulence (Fig. 7e) indicates that the increase of  
 209  $N^2$  observed in the 17-18-km layer and inside of the 80-km radius cannot be attributed to these  
 210 processes, since the sum of these two terms provided forcing for destabilization. Instead, radiation  
 211 (Fig. 7d), provided the forcing for stabilization in this region. Outside of the 80-km radius, both  
 212 advection (Fig. 7b) and vertical turbulence (Fig. 7c) provided forcing for stabilization near the  
 213 18-km level. The sum of the two terms indicates increasing  $N^2$  near the 18-km level everywhere  
 214 outside of the 80-km radius, but this stabilization is slightly weaker in the 90-120-km radial band

215 than the observed value. The addition of radiation (Fig. 7f) provides the extra forcing for stabi-  
 216 lization required to account for the observed increase in  $N^2$ . Outside of the 120-km radius, the  
 217 region of radiative forcing for stabilization slopes downward, and the increase in  $N^2$  observed near  
 218 18 km can be explained entirely by a combination of advection and vertical turbulence. The layer  
 219 of decreasing  $N^2$  observed near 17 km was forced primarily by vertical turbulence and radiation.  
 220 Within most of this region, advection provided strong forcing for stabilization, but this forcing  
 221 was outweighed by the negative  $N^2$  tendencies induced by a combination of vertical turbulence  
 222 and radiation.

## 223 5. Discussion

### 224 a. *The role of advection*

225 Advection played an important role in the tropopause-layer  $N^2$  evolution at all stages of intensi-  
 226 fication, but for brevity, this section will focus only on the RI (24-48-hour) period. To investigate  
 227 the advective processes more closely, the individual contributions of horizontal and vertical advec-  
 228 tion during the RI period are shown in Fig. 8, along with the corresponding time-mean radial and  
 229 vertical velocities and  $\theta$ . The  $N^2$  tendencies due to the two advective components (Fig. 8a,b) ex-  
 230 hibit strong cancellation, consistent with flow that is nearly isentropic. There are, however, some  
 231 regions in which flow crosses  $\theta$  surfaces; this flow accounts for all non-zero  $N^2$  tendencies due to  
 232 advection previously seen in Fig. 6b.

233 Some insight can be gained by considering the time tendency of the vertical  $\theta$  gradient due to  
 234 advection:

$$\left( \frac{\partial}{\partial t} \frac{\partial \theta}{\partial z} \right)_{adv} = -u \frac{\partial}{\partial r} \frac{\partial \theta}{\partial z} - w \frac{\partial}{\partial z} \frac{\partial \theta}{\partial z} - \frac{\partial u}{\partial z} \frac{\partial \theta}{\partial r} - \frac{\partial w}{\partial z} \frac{\partial \theta}{\partial z}. \quad (9)$$

235 The first two terms on the right-hand side of Eq. 9 represent advection of static stability by  
 236 the radial and vertical wind, respectively. These terms cannot create a maximum or a minimum;  
 237 they only act to rearrange the static stability field. Since the goal of this analysis is to understand  
 238 the processes responsible for the creation of maxima and minima in  $N^2$ , these two terms will not  
 239 be examined. The third and fourth terms represent, respectively, the tilting of isentropes in the  
 240 presence of vertical wind shear, and the spreading or compaction of isentropes through divergence  
 241 of the vertical wind. Since these terms involve gradients of velocities, they can create or eliminate  
 242 local maxima or minima in static stability. This section will focus on these two terms.

243 During the RI period, strong radial and vertical circulations developed near the tropopause,  
 244 which forced high-magnitude  $N^2$  tendencies due to advection (Fig. 8a,b). A layer of strong outflow  
 245 developed at and below the tropopause during this period, with the outflow maximum (dashed cyan  
 246 line) curving from the 14-km level at the 50-km radius to just below the 16-km level outside of  
 247 the 80-km radius (Fig. 8c). The cyan line, by definition, represents the level at which the vertical  
 248 gradient of radial velocity switched signs, with  $\partial u / \partial z > 0$  below the line and  $\partial u / \partial z < 0$  above.  
 249 Notably, the  $N^2$  tendency due to horizontal advection (Fig. 8a) also tended to switch signs very  
 250 near this line, with stabilization below the outflow maximum and destabilization above. This  
 251 suggests that vertical wind shear above and below the outflow maximum played an important  
 252 role in the  $N^2$  tendency during this time. Examination of the third term on the right-hand side  
 253 of Eq. 9 reveals that tilting of isentropes within these shear layers contributed to the strong  $N^2$   
 254 tendencies that flanked the outflow maximum. Outside of the eye and eyewall, isentropes generally  
 255 sloped upward with radius, which means that  $\theta$  decreased outward ( $\partial \theta / \partial r < 0$ ). Thus, wherever  
 256  $\partial u / \partial z > 0$ , the tilting term must force an increase in  $N^2$ , and wherever  $\partial u / \partial z < 0$ , the tilting term  
 257 must force a decrease in  $N^2$ . This is precisely the structure seen in Fig. 8a, which suggests that the  
 258 tilting term might be important near the outflow jet.

Advection of  $N^2$  by the radial wind (first term on the right-hand side of Eq. 9) also acts within the outflow jet. For example, horizontal advection provided forcing for destabilization at the 16-km level almost everywhere inside of the 140-km radius. Outside of this radius near 16 km, however, existed a region of forcing for stabilization. This switch in signs was a consequence of a reversal of the radial gradient of mean  $N^2$  near the 140-km radius (Fig. 3b). Inside of that radius,  $(\partial/\partial r)(\partial\theta/\partial z) > 0$  and  $u > 0$ , which corresponds to forcing for destabilization in Eq. 9; outside of that radius  $(\partial/\partial r)(\partial\theta/\partial z) < 0$  and  $u > 0$ , which corresponds to forcing for stabilization.

The relative importance of the first and third terms on the right-hand side of Eq. 9 is difficult to ascertain, but the structure of the mean radial velocity,  $\theta$ , and  $N^2$  fields suggests that both terms are contributing within the outflow layer.

Meanwhile in the lower stratosphere, a thin layer of 2-4 m s<sup>-1</sup> inflow developed a few hundred meters above the tropopause, similar to that which was observed in Hurricane Patricia (2015; Duran and Molinari 2018). Since the isentropes in this layer slope slightly upward with radius (i.e.  $\partial\theta/\partial r < 0$ ), this inflow acts to import lower  $\theta$  air to inner radii. There also existed strong radial gradients of mean  $N^2$  in this layer during this time (Fig. 3b), so the inflow layer must have acted to rearrange  $N^2$ . This rearrangement could not have been responsible for the overall increase in  $N^2$  during this period, however. If horizontal advection contributed to the strengthening stable layer just above the tropopause, it must have been through the tilting term. The inflow maximum near the 18-km level represents the level at which the sign of  $\partial u/\partial z$  reverses, with  $\partial u/\partial z < 0$  below and  $\partial u/\partial z > 0$  above. The third term on the right-hand side of Eq. 9 suggests that the tilting of isentropes should act to destabilize the layer below the inflow maximum and stabilize the layer above, and this was observed in Fig. 8a.

281 *b. The role of radiation*

282 During the initial spin-up period (0-24 hours; 9a), convection was not deep enough to deposit  
283 large quantities of ice near the tropopause in the mean. Due to the lack of ice particles, the  
284 radiative heating tendencies during this period (Fig. 9b) were relatively small and confined to the  
285 region above a few particularly strong convective towers. During RI (24-48 hours; Fig. 9b), the  
286 eyewall updraft strengthened and a radially-extensive cirrus canopy developed near the tropopause.  
287 The enhanced vertical gradient of ice mixing ratio at the top of the cirrus canopy induced strong  
288 diurnal-mean radiative cooling near the tropopause (9d). This cooling exceeded  $0.6 \text{ K h}^{-1}$  in some  
289 places and sloped downward from the lower stratosphere into the upper troposphere, following the  
290 top of the cirrus canopy. A small radiative warming maximum also appeared outside of the 140-km  
291 radius below this region of cooling. These results broadly agree with those of Bu et al. (2014; see  
292 their Fig. 11a), whose CM1 simulations 0.3 K net diurnally-averaged radiative cooling at the top  
293 of the cirrus canopy and radiative warming within the cloud maximized near the 200-km radius.  
294 The broad region of radiative cooling acted to destabilize the layer below the cooling maximum  
295 and stabilize the layer above, which can be seen in Fig. 6d. The small area of net radiative heating  
296 outside of the 140-km radius enhanced the destabilization in this region and produced a thin layer  
297 of stabilization in the 15-16-km layer.

298 After the TC's RI period completed (48-72 hours; Fig. 9f), strong radiative cooling remained  
299 near the tropopause at inner radii, sloping downward with the top of the cirrus canopy to below the  
300 tropopause at outer radii. Cooling rates exceeded  $1 \text{ K h}^{-1}$  just above the tropopause between the 30-  
301 and 70-km radii. These cooling rates exceeded those observed by Bu et al. (2014), a discrepancy  
302 that is likely a consequence of their larger vertical grid spacing (625 m) compared to that used here

303 (250 m), with a possible a contribution from differing radiation schemes<sup>5</sup>. Time-mean radiative  
304 warming spread from 30- to 160-km radius within the cirrus canopy. The existence of radiative  
305 cooling overlying radiative warming in this region led to radiatively-forced destabilization at and  
306 below the tropopause, as was observed in Fig. 7d. Below the warming layer existed a region of  
307 forcing for stabilization, while a much stronger region of forcing for destabilization existed above  
308 the cooling maximum in the lower stratosphere.

309 The results herein suggest that radiative heating tendencies played an important role in destabi-  
310 lizing the upper troposphere and stabilizing the lower stratosphere after the cirrus canopy devel-  
311 oped and persisted during and after RI.

### 312 *c. The role of turbulent mixing*

313 Although vertical turbulence always acts to eliminate vertical gradients of  $\theta$ , this adjustment  
314 toward a neutral state only occurs where the mixing takes place. If turbulence occurs in a stably-  
315 stratified layer, it will act to decrease  $\theta$  at the top of the layer and increase it below. Just above and  
316 just below the mixed layer, however, the  $\theta$  profile remains undisturbed. Consequently, although  
317 turbulent mixing acts to decrease  $\partial\theta/\partial z$  in the layer in which it is occurring, it actually increases  
318  $\partial\theta/\partial z$  just below and just above the layer. These vertical gradients of turbulent mixing are quite  
319 important, particularly on the flanks of the upper-tropospheric outflow jet.

320 Diurnal variability of of static stability in the upper troposphere is an interesting area of future  
321 research.

---

<sup>5</sup>Bu et al. (2014) employed the NASA-Goddard radiation scheme for their CM1 simulations, whereas RRTMG is used in the present paper. They did use the RRTMG radiation scheme alongside the Thompson microphysics parameterization for their HWRF simulations, but those simulations also produced smaller radiative tendencies than those seen here (see their Fig. 5a), suggesting that vertical resolution accounts for most of the difference in radiative heating rates.



322 Bu et al. did not see a lower-stratospheric inflow layer, likely due to their 625-m grid spacing.  
323 If we want to resolve properly the radiative cooling at the top of the cirrus canopy and the lower-  
324 stratospheric inflow layer, we must have sufficient vertical resolution in the tropopause layer. Our  
325 100-m grid spacing here may not even be sufficient, given how shallow the layer is! Did my no-  
326 CRF simulation show a lower-stratospheric inflow layer?? If not, that's strong evidence supporting  
327 the role of radiation in producing the descending inflow layer above the tropopause.

328 *Acknowledgments.* We are indebted to George Bryan for his continued development and support  
329 of Cloud Model 1. We also thank Jeffrey Kepert, Robert Fovell, and Erika Navarro for helpful  
330 conversations related to this work. This research was supported by NSF Grant #1636799.

## 331 APPENDIX

### 332 Sensitivity experiments

333 The simulations exhibited some sensitivity to the initial thermodynamic profile and the prescribed  
334 vertical mixing length. Although the details of the intensification and the tropopause-layer  $N^2$  evo-  
335 lution varied when these quantities were changed, the conclusions of the paper remain unchanged.

#### 336 *a. Sensitivity to the initial thermodynamic profile*

337 A number of sensitivity experiments were conducted using a variety of initial soundings. Chang-  
338 ing the initial temperature and humidity profiles affected the timing of the onset of organized deep  
339 convection and the rapidity of intensification. In all simulations, however, convection eventually  
340 penetrated to the tropopause, at which time vertical turbulence and radiation combined with ad-  
341 vection to adjust the  $N^2$  profile toward that which was observed in the control run. By the end of  
342 the RI period in every simulation, all three processes were actively modifying the  $N^2$  profile near  
343 the tropopause.

*b. Sensitivity to the vertical mixing length*

The intensity of parameterized turbulence is highly dependent on a prescribed length scale. Since there is no theoretical or observational guidance for the selection of this mixing length, the value used in the control run (100 m) is based on the sensitivity experiments of Bryan (2012). Since the vertical eddy viscosity varies linearly with the vertical mixing length, prescribing a smaller mixing length produces smaller  $\theta$  tendencies due to turbulence. Even with a mixing length on the low end of those tested by Bryan (2012), however, turbulence still plays a role in the tropopause-layer  $N^2$  evolution. FIG shows the  $N^2$  evolution in a simulation identical to the control run, except with a vertical mixing length of 50 m rather than 100 m. DESCRIPTION OF THE FIGURE

**References**

- Bryan, G. H., 2012: Effects of surface exchange coefficients and turbulence length scales on the intensity and structure of numerically simulated hurricanes. *Mon. Wea. Rev.*, **140**, 1125–1143.
- Bryan, G. H., and R. Rotunno, 2009: The maximum intensity of tropical cyclones in axisymmetric numerical model simulations. *Mon. Wea. Rev.*, **137**, 1770–1789.
- Bu, Y. P., R. G. Fovell, and K. L. Corbosiero, 2014: Influence of cloud-radiative forcing on tropical cyclone structure. *J. Atmos. Sci.*, **71**, 1644–1622.
- Doyle, J. D., and Coauthors, 2017: A view of tropical cyclones from above: The Tropical Cyclone Intensity (TCI) Experiment. *Bull. Amer. Meteor. Soc.*, **98**, 2113–2134.
- Duran, P., and J. Molinari, 2018: Dramatic inner-core tropopause variability during the rapid intensification of Hurricane Patricia (2015). *Mon. Wea. Rev.*, **146**, 119–134.

- 365 Emanuel, K., 2012: Self-stratification of tropical cyclone outflow. Part II: Implications for storm  
366 intensification. *J. Atmos. Sci.*, **69**, 988–996.
- 367 Emanuel, K., and R. Rotunno, 2011: Self-stratification of tropical cyclone outflow. Part I: Impli-  
368 cations for storm structure. *J. Atmos. Sci.*, **68**, 2236–2249.
- 369 Iacono, M. J., J. S. Delamere, E. J. Mlawer, M. W. Shephard, S. A. Clough, and W. D. Collins,  
370 2008: Radiative forcing by long-lived greenhouse gases: Calculations with the AER radiative  
371 transfer models. *J. Geophys. Res.*, **113** (D13103).
- 372 Kepert, J. D., J. Schwendike, and H. Ramsay, 2016: Why is the tropical cyclone boundary layer  
373 not "well mixed"? *J. Atmos. Sci.*, **73**, 957–973.
- 374 Kimberlain, T. B., E. S. Blake, and J. P. Cangialosi, 2016: Tropical cyclone report: Hurricane  
375 Patricia. National Hurricane Center. [Available online at [www.nhc.noaa.gov](http://www.nhc.noaa.gov)].
- 376 Komaromi, W. A., and J. D. Doyle, 2017: Tropical cyclone outflow and warm core structure as  
377 revealed by HS3 dropsonde data. *Mon. Wea. Rev.*, **145**, 1339–1359.
- 378 Markowski, P. M., and G. H. Bryan, 2016: LES of laminar flow in the PBL: A potential problem  
379 for convective storm simulations. *Mon. Wea. Rev.*, **144**, 1841–1850.
- 380 Ohno, T., and M. Satoh, 2015: On the warm core of a tropical cyclone formed near the tropopause.  
381 *J. Atmos. Sci.*, **72**, 551–571.
- 382 Rogers, R. F., S. Aberson, M. M. Bell, D. J. Cecil, J. D. Doyle, J. Morgerman, L. K. Shay, and  
383 C. Velden, 2017: Re-writing the tropical record books: The extraordinary intensification of  
384 Hurricane Patricia (2015). *Bull. Amer. Meteor. Soc.*, **98**, 2091–2112.

385 Rotunno, R., and K. A. Emanuel, 1987: An air-sea interaction theory for tropical cyclones. Part II:  
386 Evolutionary study using a nonhydrostatic axisymmetric numerical model. *J. Atmos. Sci.*, **44**,  
387 542–561.

388 Stern, D. P., and F. Zhang, 2013: How does the eye warm? Part I: A potential temperature budget  
389 analysis of an idealized tropical cyclone. *J. Atmos. Sci.*, **70**, 73–89.

390 Thompson, G., R. M. Rasmussen, and K. Manning, 2004: Explicit forecasts of winter precipitation  
391 using an improved bulk microphysics scheme. Part I: Description and sensitivity analysis. *Mon.*  
392 *Wea. Rev.*, **132**, 519–542.

## LIST OF FIGURES

<b>Fig. 1.</b>	The maximum 10-m wind speed (top panel; $\text{m s}^{-1}$ ) and minimum sea-level pressure (bottom panel; hPa) in the simulated storm (blue lines) and from Hurricane Patricia's best track (red stars).	22
<b>Fig. 2.</b>	Left panels: Twenty-four-hour changes in squared Brunt-Väisälä frequency ( $N^2$ ; $10^{-4} \text{ s}^{-2}$ ) over (a) 0-24 hours, (b) 24-48 hours, (c) 48-72 hours. Middle Panels: The $N^2$ change over the same time periods computed using Eqs. 4-6, Right Panels: The budget residual over the same time periods, computed by subtracting the budget change (middle column) from the model change (left column).	23
<b>Fig. 3.</b>	Twenty-four-hour averages of squared Brunt-Väisälä frequency ( $N^2$ ; $10^{-4} \text{ s}^{-2}$ ) over (a) 0-24 hours, (b) 24-48 hours, (c) 48-72 hours. Orange lines represent the cold-point tropopause averaged over the same time periods.	24
<b>Fig. 4.</b>	Time series of the contribution of each of the budget terms to the time tendency of the squared Brunt-Väisälä frequency ( $N^2$ ; $10^{-4} \text{ s}^{-2}$ ). For each budget term, the absolute value of the $N^2$ tendency is averaged temporally over 1-hour periods (using output every minute), and spatially in a region extending from 0 to 200 km radius and 14 to 21 km altitude.	25
<b>Fig. 5.</b>	(a) Total change in $N^2$ over the 0-24-hour period ( $10^{-4} \text{ s}^{-2} (24 \text{ h})^{-1}$ ) and the contributions to that change from (b) the sum of horizontal and vertical advection, (c) vertical turbulence, (d) longwave and shortwave radiation, (e) the sum of horizontal advection, vertical advection, and vertical turbulence, and (f) the sum of horizontal advection, vertical advection, vertical turbulence, and longwave and shortwave radiation.	26
<b>Fig. 6.</b>	As in Fig. 5, but for the 24-48-hour period.	27
<b>Fig. 7.</b>	As in Fig. 5, but for the 48-72-hour period.	28
<b>Fig. 8.</b>	The contribution to the change in $N^2$ over the 24-48-hour period ( $10^{-4} \text{ s}^{-2} (24 \text{ h})^{-1}$ ) by (a) horizontal advection and (b) vertical advection. (c) The radial velocity ( $\text{m s}^{-1}$ ; filled contours), potential temperature (K; thick black contours), cold-point tropopause height (orange line), and level of maximum outflow (dashed cyan line) averaged over the 24-48-hour period. (d) The vertical velocity ( $\text{cm s}^{-1}$ ; filled contours), potential temperature (K; thick black contours), and cold-point tropopause height (orange line) averaged over the 24-48-hour period.	29
<b>Fig. 9.</b>	Ice mixing ratio ( $\text{g kg}^{-1}$ ) and cold-point tropopause height (orange lines) averaged over (a) 0-24 hours, (c) 24-48 hours, and (e) 48-72 hours. Radiative heating rate ( $\text{K h}^{-1}$ ) and cold-point tropopause height (orange lines) averaged over (b) 0-24 hours, (d) 24-48 hours, and (f) 48-72 hours.	30
<b>Fig. 10.</b>	Vertical eddy diffusivity ( $\text{m}^2 \text{ s}^{-2}$ ; filled contours), cold-point tropopause height (cyan lines), and radial velocity ( $\text{m s}^{-1}$ ; thick black lines) averaged over (a) 0-24 hours, (b) 24-48 hours, and (c) 48-72 hours.	31

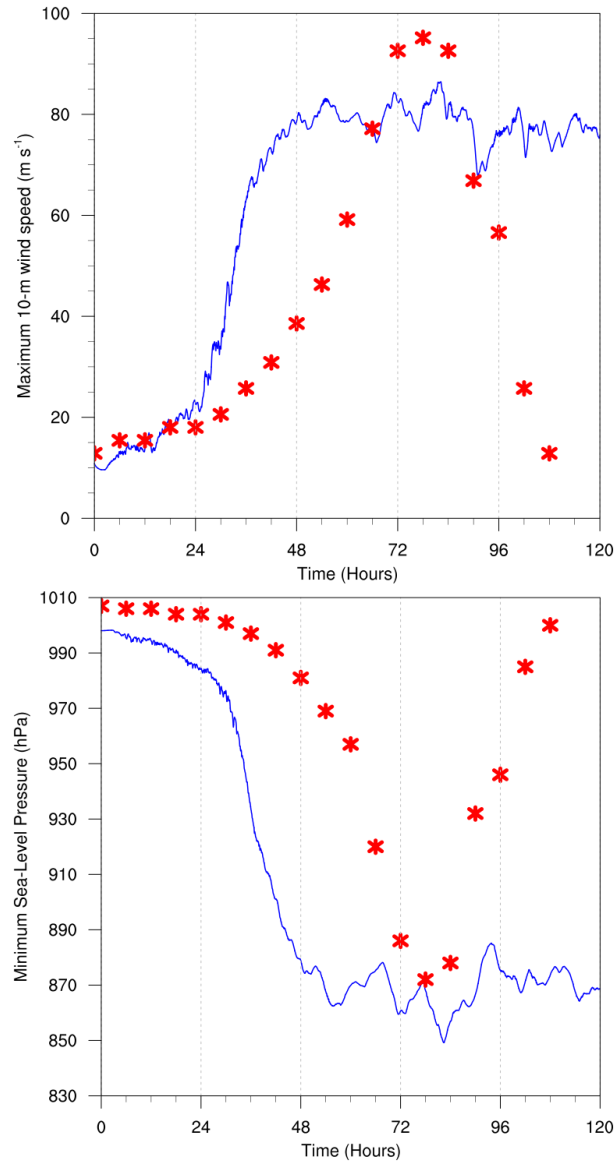
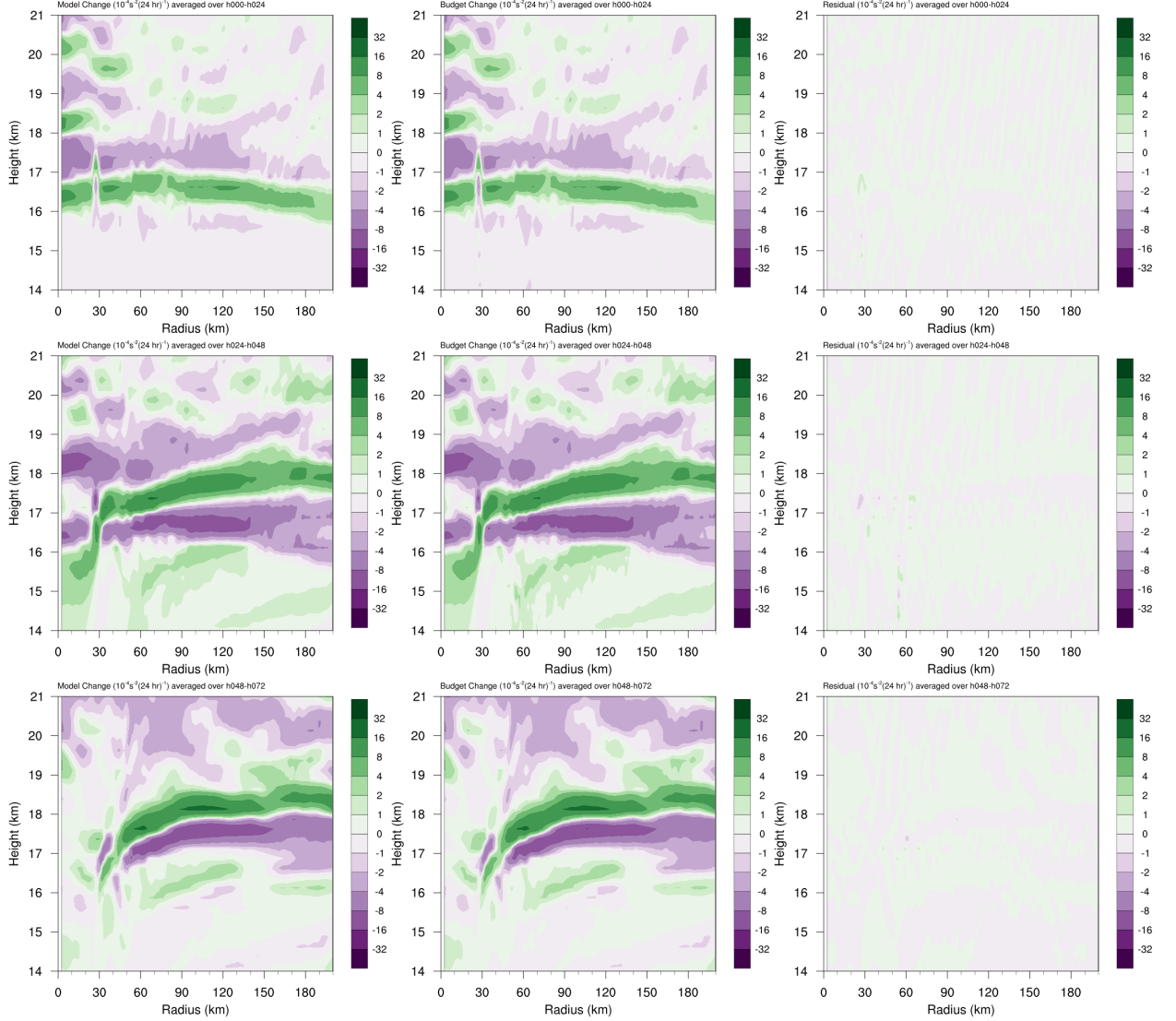


FIG. 1. The maximum 10-m wind speed (top panel;  $\text{m s}^{-1}$ ) and minimum sea-level pressure (bottom panel; hPa) in the simulated storm (blue lines) and from Hurricane Patricia's best track (red stars).



432 FIG. 2. Left panels: Twenty-four-hour changes in squared Brunt-Väisälä frequency ( $N^2$ ;  $10^{-4} \text{ s}^{-2}$ ) over (a) 0-  
 433 24 hours, (b) 24-48 hours, (c) 48-72 hours. Middle Panels: The  $N^2$  change over the same time periods computed  
 434 using Eqs. 4-6, Right Panels: The budget residual over the same time periods, computed by subtracting the  
 435 budget change (middle column) from the model change (left column).

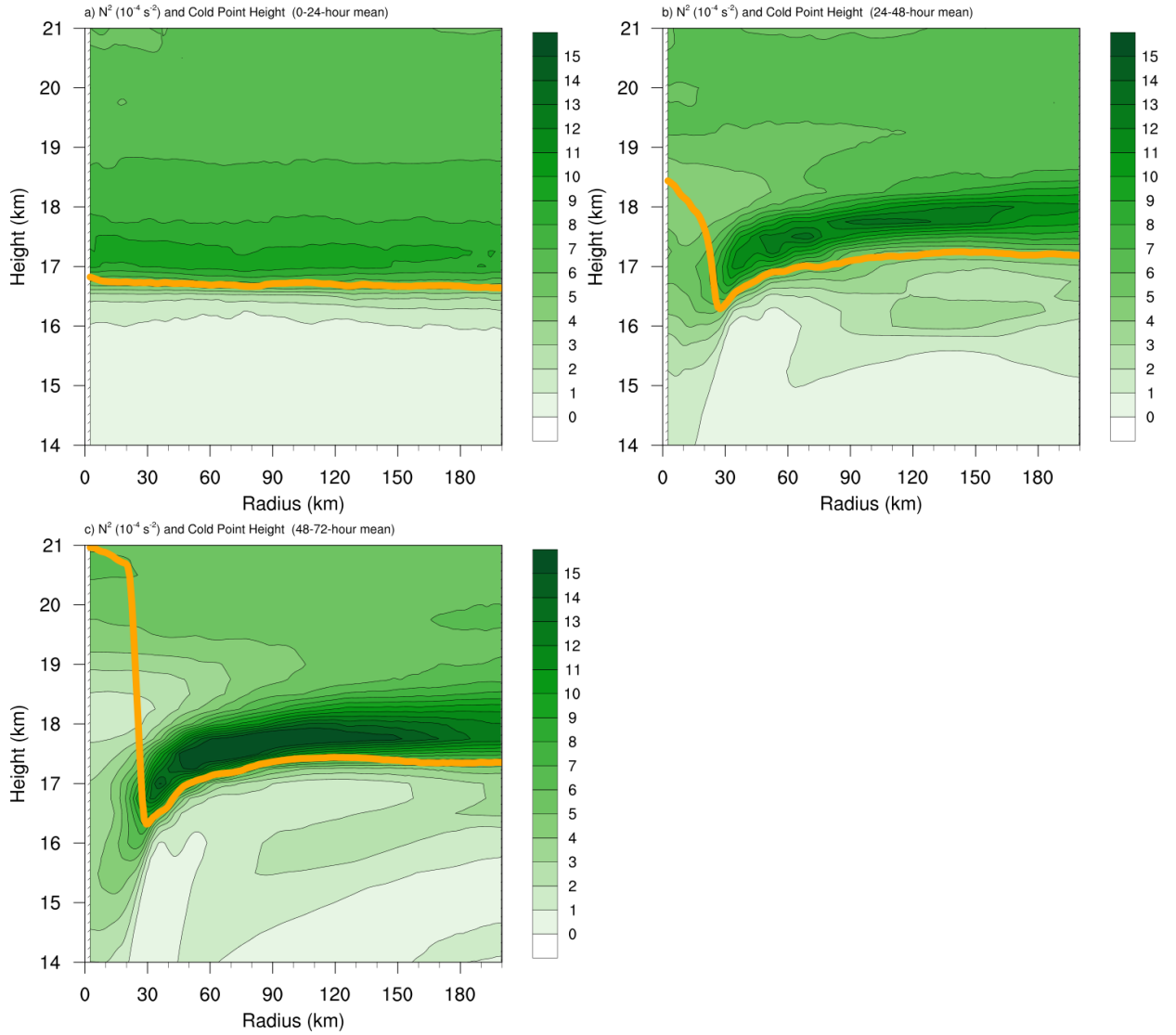


FIG. 3. Twenty-four-hour averages of squared Brunt-Väisälä frequency ( $N^2$ ;  $10^{-4} \text{ s}^{-2}$ ) over (a) 0-24 hours, (b) 24-48 hours, (c) 48-72 hours. Orange lines represent the cold-point tropopause averaged over the same time periods.



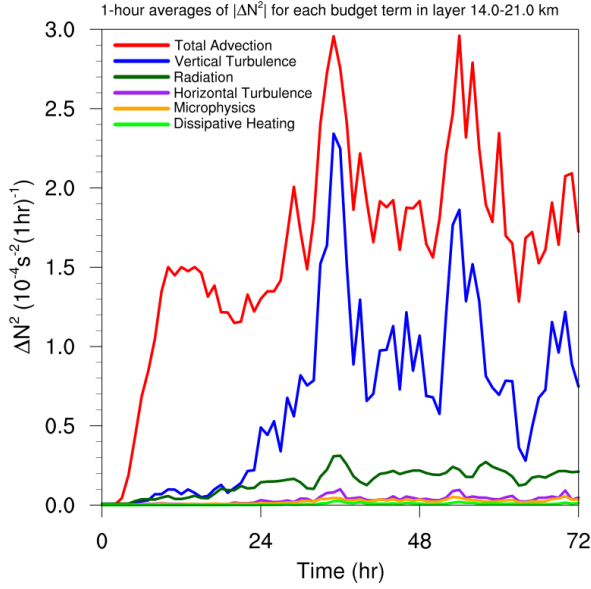
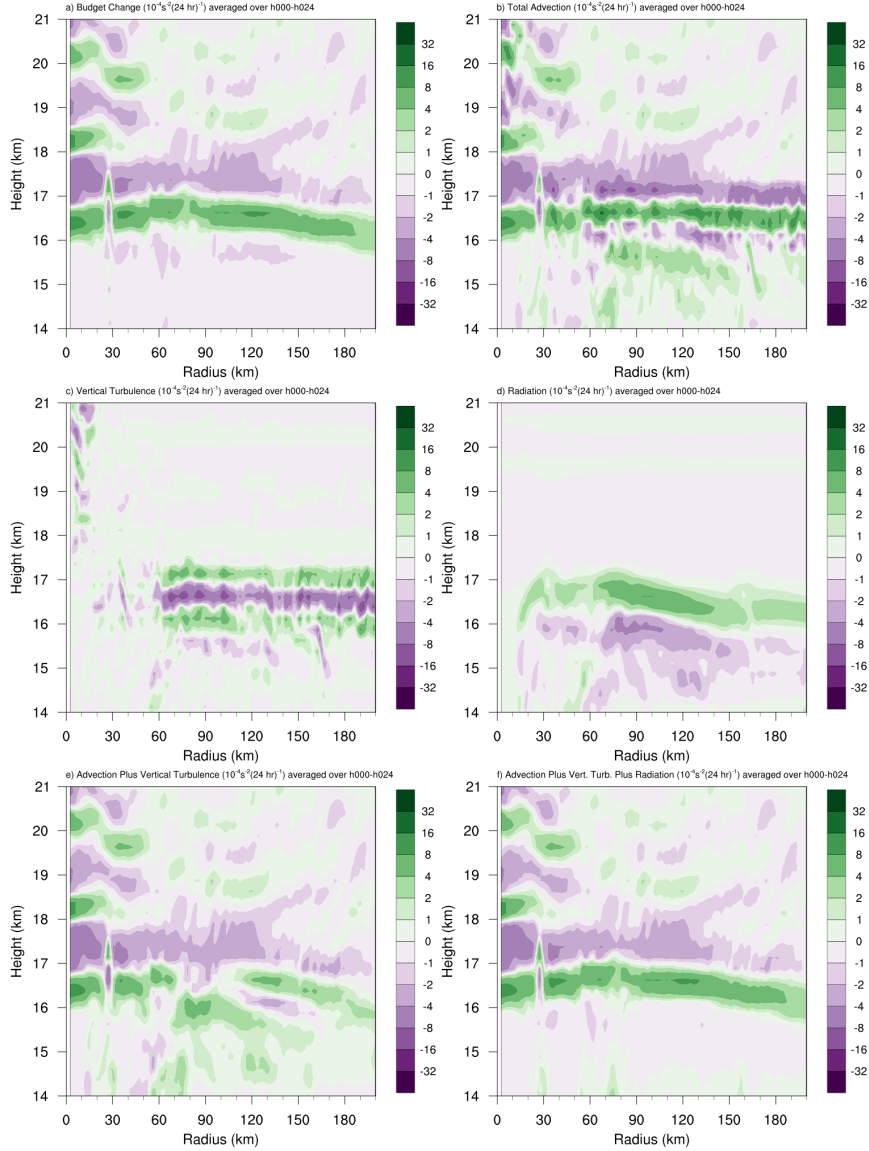


FIG. 4. Time series of the contribution of each of the budget terms to the time tendency of the squared Brunt-Väisälä frequency ( $N^2$ ;  $10^{-4} \text{ s}^{-2}$ ). For each budget term, the absolute value of the  $N^2$  tendency is averaged temporally over 1-hour periods (using output every minute), and spatially in a region extending from 0 to 200 km radius and 14 to 21 km altitude.



443 FIG. 5. (a) Total change in  $N^2$  over the 0-24-hour period ( $10^{-4} \text{ s}^{-2} (24 \text{ h})^{-1}$ ) and the contributions to that change  
 444 from (b) the sum of horizontal and vertical advection, (c) vertical turbulence, (d) longwave and shortwave  
 445 radiation, (e) the sum of horizontal advection, vertical advection, and vertical turbulence, and (f) the sum of  
 446 horizontal advection, vertical advection, vertical turbulence, and longwave and shortwave radiation.

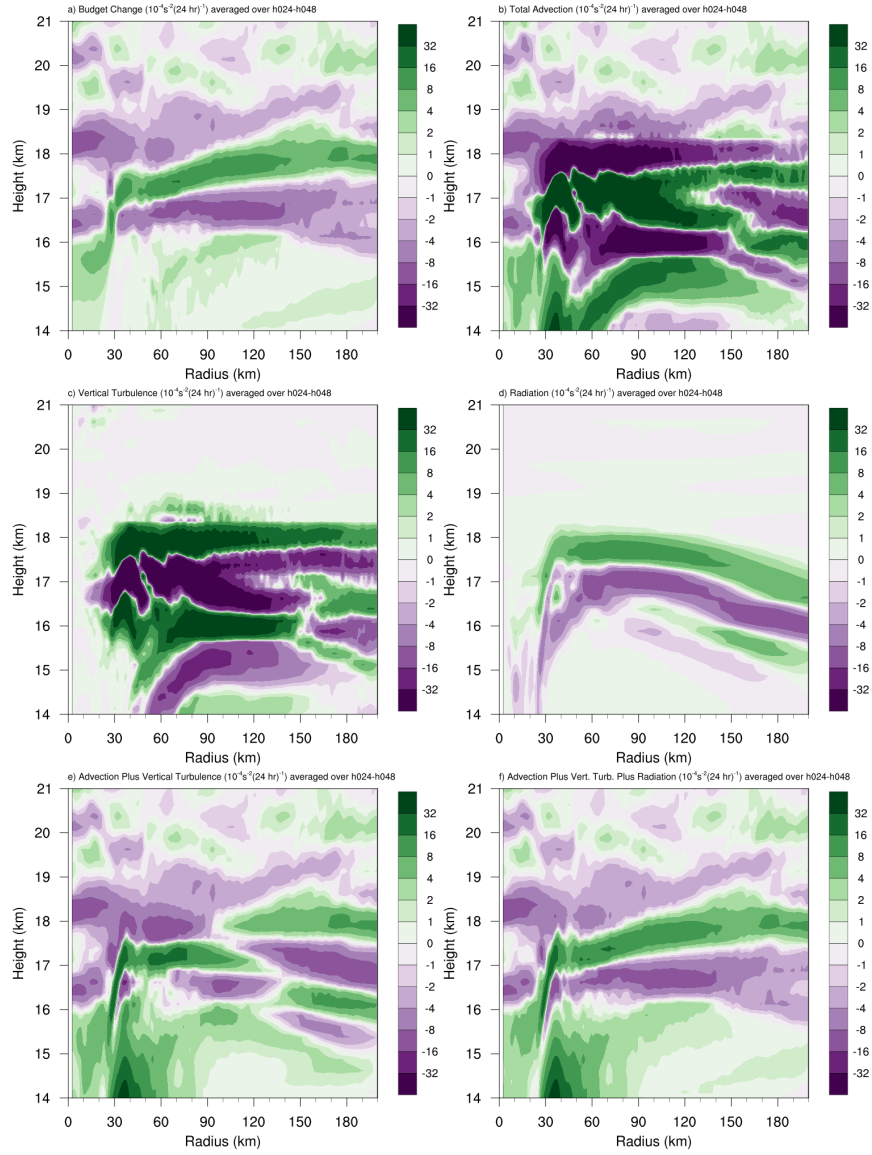


FIG. 6. As in Fig. 5, but for the 24-48-hour period.

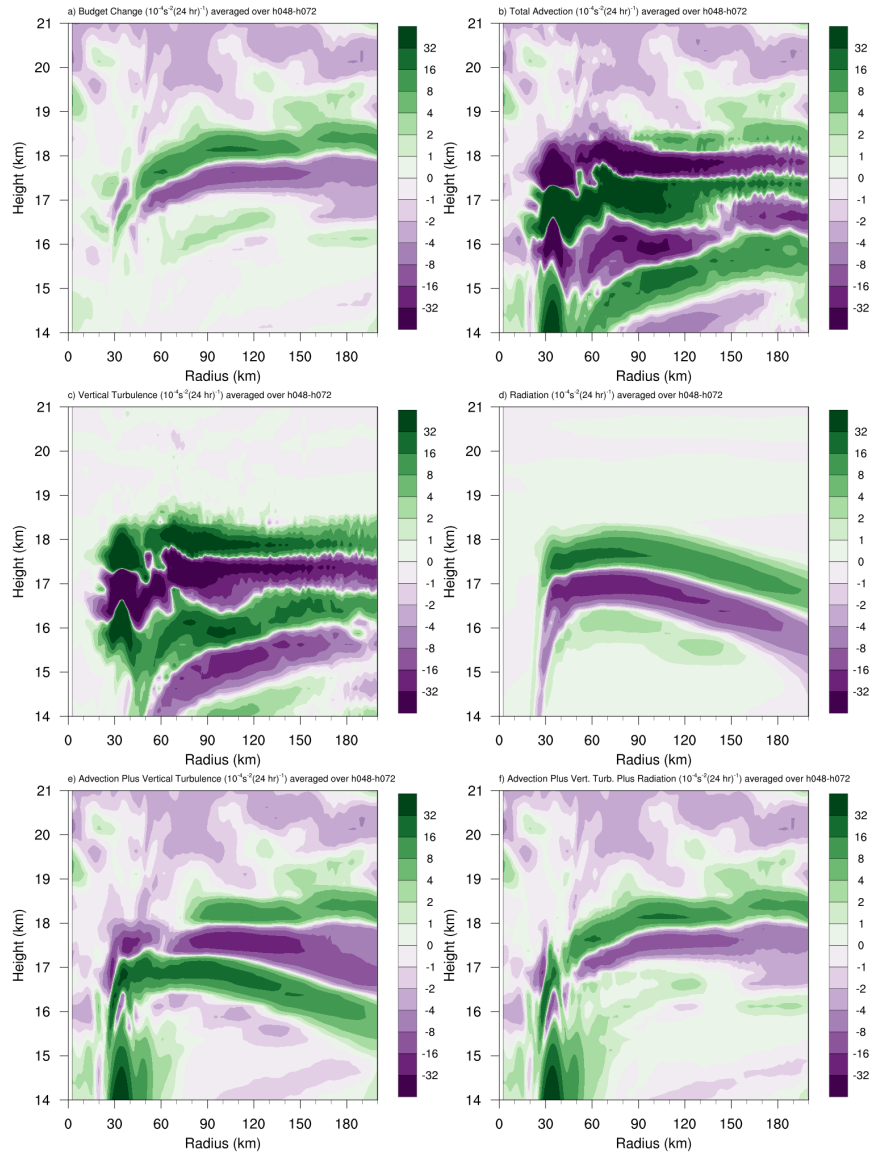


FIG. 7. As in Fig. 5, but for the 48-72-hour period.

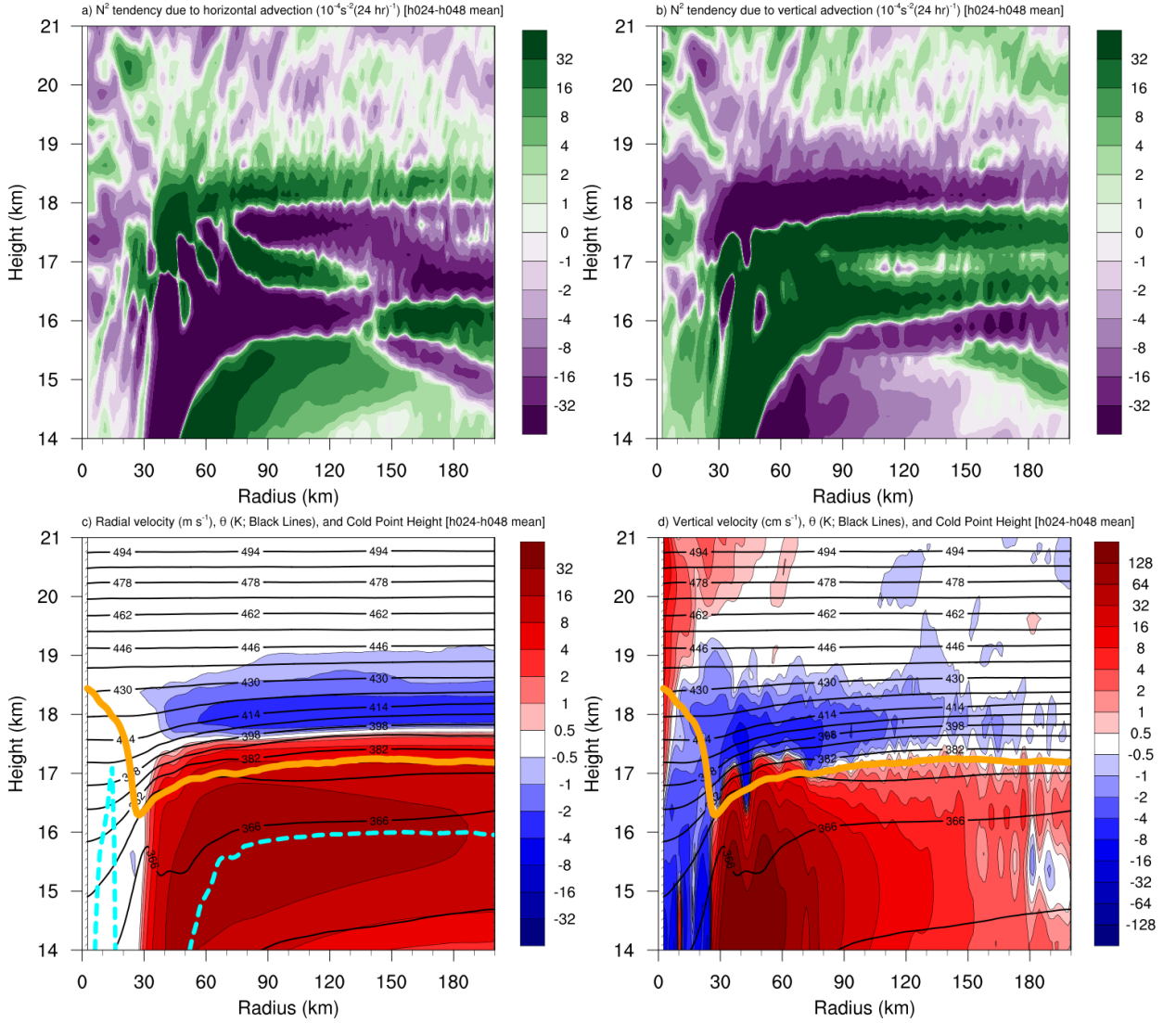


FIG. 8. The contribution to the change in  $N^2$  over the 24-48-hour period ( $10^{-4} \text{s}^{-2} (24 \text{ h})^{-1}$ ) by (a) horizontal advection and (b) vertical advection. (c) The radial velocity ( $\text{m s}^{-1}$ ; filled contours), potential temperature (K; thick black contours), cold-point tropopause height (orange line), and level of maximum outflow (dashed cyan line) averaged over the 24-48-hour period. (d) The vertical velocity ( $\text{cm s}^{-1}$ ; filled contours), potential temperature (K; thick black contours), and cold-point tropopause height (orange line) averaged over the 24-48-hour period.

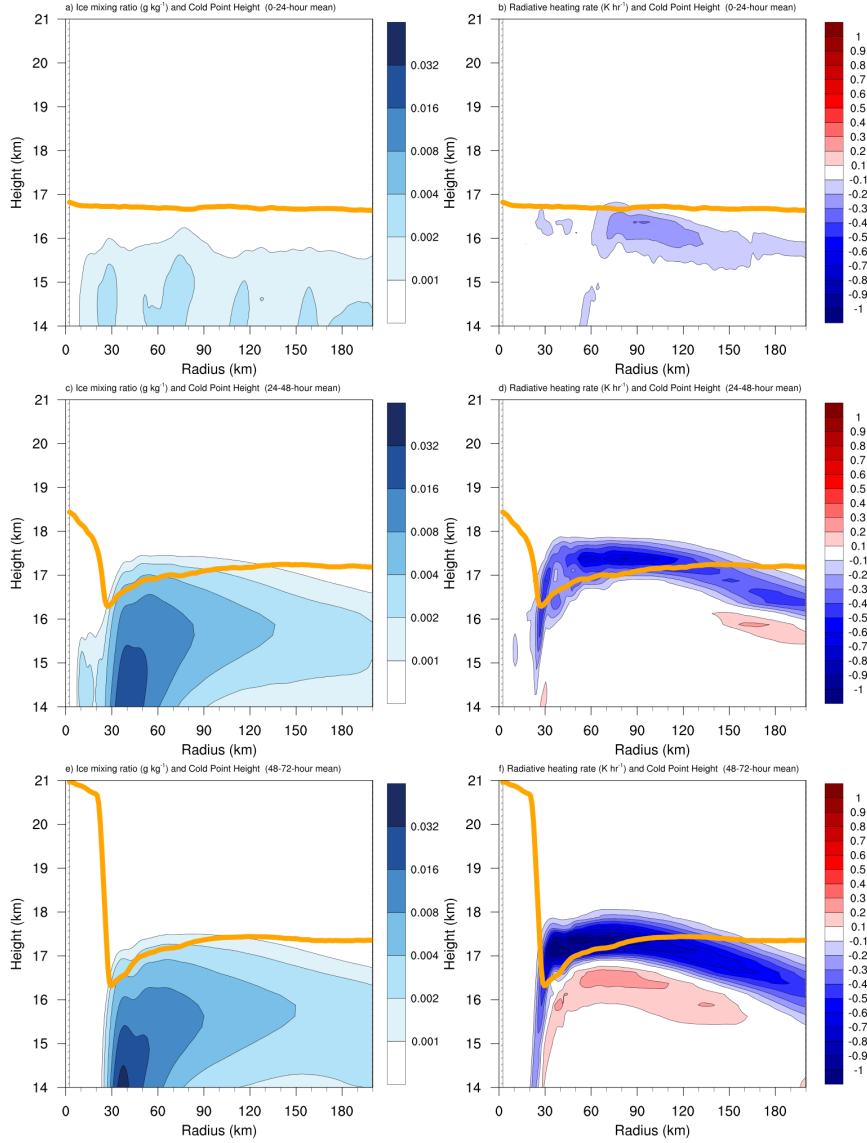


FIG. 9. Ice mixing ratio ( $\text{g kg}^{-1}$ ) and cold-point tropopause height (orange lines) averaged over (a) 0-24 hours, (c) 24-48 hours, and (e) 48-72 hours. Radiative heating rate ( $\text{K h}^{-1}$ ) and cold-point tropopause height (orange lines) averaged over (b) 0-24 hours, (d) 24-48 hours, and (f) 48-72 hours.

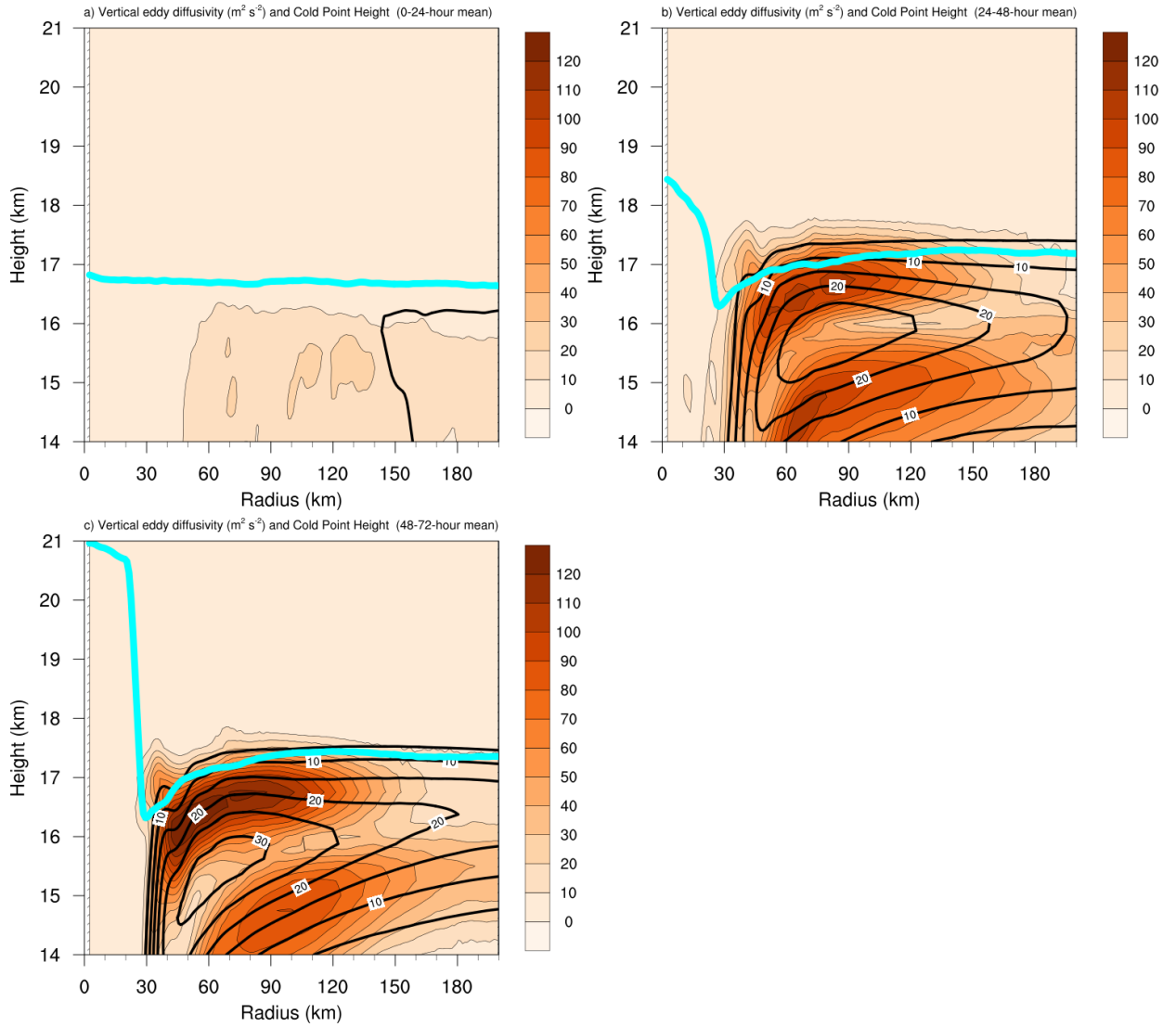


FIG. 10. Vertical eddy diffusivity ( $\text{m}^2 \text{s}^{-2}$ ; filled contours), cold-point tropopause height (cyan lines), and radial velocity ( $\text{m s}^{-1}$ ; thick black lines) averaged over (a) 0-24 hours, (b) 24-48 hours, and (c) 48-72 hours.